

Higgs Portal Vector Dark Matter : Revisited

Seungwon Baek,^a P. Ko,^a Wan-II Park^a and Eibun Senaha^a

^a*School of Physics, KIAS,
Seoul 130-722, Korea*

E-mail: sbaek1560@gmail.com, pko@kias.re.kr, wipark@kias.re.kr,
senaha@kias.re.kr

ABSTRACT: We revisit the Higgs portal vector dark matter model including a hidden sector Higgs field that generates the mass of the vector dark matter. The model becomes renormalizable and has two scalar bosons, the mixtures of the standard model (SM) Higgs and the hidden sector Higgs bosons. The strong bound from direct detection such as XENON100 is evaded due to the cancellation mechanism between the contributions from two scalar bosons. As a result, the model becomes still viable in large range of dark matter mass, contrary to some claims in the literature. The Higgs properties are also affected, the signal strengths for the Higgs boson search being universally suppressed relative to the SM value, which could be tested at the LHC in the future.

KEYWORDS:

Contents

1	Introduction	1
2	The model Lagrangian for vector dark matter	3
3	Phenomenology	3
3.1	Dark matter phenomenology	3
3.2	Collider phenomenology	7
3.3	The EFT as a limit of the full theory for $m_2 \rightarrow \infty$	9
4	Vacuum stability and perturbativity of Higgs quartic couplings	12
5	Conclusions	14
A	One-loop β functions of Higgs quartic couplings	16

1 Introduction

The so-called Higgs portal cold dark matter (CDM) model is an interesting possibility for the nonbaryonic dark matter of the universe. The dark matter fields are assumed to be the standard model (SM) gauge singlets, and could be a scalar (S), a singlet fermion (ψ) or a vector boson (X) depending on their spin. The Lagrangian of these CDM's are usually taken as [1–4]

$$\mathcal{L}_{\text{scalar}} = \frac{1}{2}\partial_\mu S \partial^\mu S - \frac{1}{2}m_S^2 S^2 - \frac{\lambda_{HS}}{2}H^\dagger H S^2 - \frac{\lambda_S}{4}S^4 \quad (1.1)$$

$$\mathcal{L}_{\text{fermion}} = \bar{\psi} [i\gamma \cdot \partial - m_\psi] \psi - \frac{\lambda_{H\psi}}{\Lambda} H^\dagger H \bar{\psi} \psi \quad (1.2)$$

$$\mathcal{L}_{\text{vector}} = -\frac{1}{4}X_{\mu\nu}X^{\mu\nu} + \frac{1}{2}m_X^2 X_\mu X^\mu + \frac{1}{4}\lambda_X (X_\mu X^\mu)^2 + \frac{1}{2}\lambda_{HX}H^\dagger H X_\mu X^\mu. \quad (1.3)$$

Dark matter fields (S, ψ, X_μ) are assumed to be odd under some discrete Z_2 symmetry: $(S, \psi, X_\mu) \rightarrow -(S, \psi, X_\mu)$ in order to guarantee the stability of CDM. This symmetry removes the kinetic mixing between the $X_{\mu\nu}$ and the $U(1)_Y$ gauge field $B^{\mu\nu}$, making X_μ stable.

The scalar CDM model (1.1) is satisfactory both theoretically and phenomenologically, as long as Z_2 symmetry is unbroken. The model is renormalizable and can be considered to high energy scale as long as the Landau pole is not hit. A large region of parameter space is still allowed by the relic density and direct detection experiments [3]. On the other hand, the other two cases have problems.

Let us first consider the fermionic CDM model (1.2). This model is nonrenormalizable, and has to be UV completed. The simplest way to achieve the UV completion of (1.2) is to

introduce a real singlet scalar field as proposed in Ref. [5, 6] by some of us. We observed that there are two Higgs-like scalar bosons which interfere destructively in the spin-independent cross section of the singlet fermion CDM on nucleon. The strong constraint from direct detection experiments such as XENON100 [7] or CDMS [8] can be relaxed significantly. On the other hand, the effective field theory (EFT) based on the Lagrangian (1.2) is strongly constrained for DM masses below about 2 TeV [1–3], although the EFT with pseudo-scalar Higgs portal suggested in [4] can be still consistent with the current direct search bound even for light DM masses. The decoupling of the 2nd scalar boson occurs rather slowly, since the mass mixing between the SM Higgs boson and the new singlet scalar is due to the dim-2 operator [6]. Also the mixing between two scalar bosons makes the signal strength of two physical Higgs-like bosons less than one, and make it difficult to detect both of them at the LHC. Since there is now an evidence for a new boson at 125 GeV at the LHC [9, 10], the 2nd scalar boson in the singlet fermion DM model is very difficult to be observed at the LHC because its signal strength is much less than 1 [6, 11]. Also an extra singlet scalar solves the vacuum instability problem for $m_H = 125$ GeV in the SM [11–13], making the electroweak (EW) vacuum stable up to Planck scale for $m_t = 173.2$ GeV. These phenomena would be very generic in general hidden sector DM models [14]. In short, it is very important to consider a renormalizable model when one considers the phenomenology of a singlet fermion CDM.

Now let us turn to the Higgs portal vector dark matter described by (1.3) [1–3]. This model is very simple, compact and seemingly renormalizable since it has only dim-2 and dim-4 operators. However, it is not really renormalizable and violates unitarity, just like the intermediate vector boson model for massive weak gauge bosons before Higgs mechanism was developed. The Higgs portal VDM model based on (1.3) is a sort of an effective Lagrangian which has to be UV completed. It lacks the dark Higgs field, $\Phi(x)$, that would generate the dark gauge field mass and will mix with the SM Higgs field, $H(x)$, after $U(1)_X$ symmetry breaking. Therefore the model (1.3) does not capture dark matter or Higgs boson phenomenology correctly. It is the purpose of this work to propose a simple UV completion of the model (1.3) with hidden sector $U(1)_X$ gauge symmetry (see also Ref. [15] for a similar approach), and deduce the correct phenomenology of vector CDM and two Higgs-like scalar bosons. Vector dark matter models in extended gauge symmetries can be found in [16]. Qualitative aspects of our model are similar to those presented in Ref.s [6, 11], although there are some quantitative differences due to the vector nature of the CDM.

This work is organized as follows. In Sec. 2, we define the model by including the hidden sector Higgs field that generates the vector dark matter mass by the usual Higgs mechanism. Then we present dark matter and collider phenomenology in the following section. We also compare the full theory with the EFT, and discuss the region in which the EFT approach is valid. The vacuum structure and the vacuum stability issues are discussed in Sec. 4, and the results are summarized in Sec. 5.

2 The model Lagrangian for vector dark matter

Let us consider a vector boson dark matter, X_μ , which is assumed to be a gauge boson associated with Abelian dark gauge symmetry $U(1)_X$. The simplest model will be without any matter fields charged under $U(1)_X$ except for a complex scalar, Φ , whose VEV will generate the mass for X_μ (see also Ref. [15]):

$$\begin{aligned} \mathcal{L}_{VDM} = & -\frac{1}{4}X_{\mu\nu}X^{\mu\nu} + (D_\mu\Phi)^\dagger(D^\mu\Phi) - \lambda_\Phi\left(\Phi^\dagger\Phi - \frac{v_\Phi^2}{2}\right)^2 \\ & - \lambda_{H\Phi}\left(H^\dagger H - \frac{v_H^2}{2}\right)\left(\Phi^\dagger\Phi - \frac{v_\Phi^2}{2}\right), \end{aligned} \quad (2.1)$$

in addition to the SM Lagrangian which includes the Higgs potential term

$$\Delta\mathcal{L}_{SM} = -\lambda_H\left(H^\dagger H - \frac{v_H^2}{2}\right)^2. \quad (2.2)$$

The covariant derivative is defined as

$$D_\mu\Phi = (\partial_\mu + ig_X Q_\Phi X_\mu)\Phi,$$

where $Q_\Phi \equiv Q_X(\Phi)$ is the $U(1)_X$ charge of Φ and we will take $Q_\Phi = 1$ throughout the paper.

Assuming that the $U(1)_X$ -charged complex scalar Φ develops a nonzero VEV, v_Φ , and thus breaks $U(1)_X$ spontaneously,

$$\Phi = \frac{1}{\sqrt{2}}(v_\Phi + \varphi(x)).$$

Therefore the Abelian vector boson X_μ gets mass $M_X = g_X|Q_\Phi|v_\Phi$, and the hidden sector Higgs field (or dark Higgs field) $\varphi(x)$ will mix with the SM Higgs field $h(x)$ through Higgs portal of the $\lambda_{H\Phi}$ term. The mixing matrix O between the two scalar fields is defined as

$$\begin{pmatrix} h \\ \varphi \end{pmatrix} = O \begin{pmatrix} H_1 \\ H_2 \end{pmatrix} \equiv \begin{pmatrix} c_\alpha & s_\alpha \\ -s_\alpha & c_\alpha \end{pmatrix} \begin{pmatrix} H_1 \\ H_2 \end{pmatrix}, \quad (2.3)$$

where $s_\alpha(c_\alpha) \equiv \sin\alpha(\cos\alpha)$, h, φ are the interaction eigenstates and $H_i(i = 1, 2)$ are the mass eigenstates with masses m_i . The mass matrix in the basis (h, φ) can be written in terms either of Lagrangian parameters or of the physical parameters as follows:

$$\begin{pmatrix} 2\lambda_H v_H^2 & \lambda_{H\Phi} v_H v_\Phi \\ \lambda_{H\Phi} v_H v_\Phi & 2\lambda_\Phi v_\Phi^2 \end{pmatrix} = \begin{pmatrix} m_1^2 c_\alpha^2 + m_2^2 s_\alpha^2 & (m_2^2 - m_1^2) s_\alpha c_\alpha \\ (m_2^2 - m_1^2) s_\alpha c_\alpha & m_1^2 s_\alpha^2 + m_2^2 c_\alpha^2 \end{pmatrix}. \quad (2.4)$$

3 Phenomenology

3.1 Dark matter phenomenology

The observed present cold dark matter density, $\Omega_{\text{CDM}}h^2 \simeq 0.1123 \pm 0.0035$ [18], is approximately related to the thermally averaged annihilation cross section at freeze-out temperature, $\langle\sigma v\rangle_{\text{fz}}$, as

$$\Omega_{\text{CDM}}h^2 = \frac{3 \times 10^{-27} \text{cm}^3/\text{s}}{\langle\sigma v\rangle_{\text{fz}}}. \quad (3.1)$$

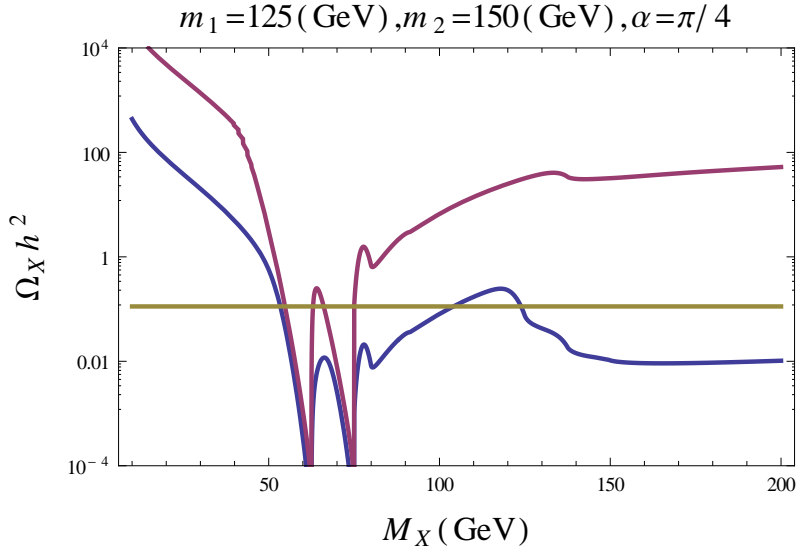


Figure 1. The thermal relic density $\Omega_X h^2$ of the vector dark matter as a function of the dark matter mass, M_X . For this plot we fixed $m_1 = 125$ GeV, $m_2 = 150$ GeV, $\alpha = \pi/4$ and the purple (blue) line corresponds to $g_X = 0.05$ (0.5). The horizontal line is the central value of the current relic density $\Omega_X h^2 = 0.1123$ [18].

So we require $\langle \sigma v \rangle_{\text{fz}} \approx 3 \times 10^{-26} \text{cm}^3/\text{s}$ to obtain the correct relic density. We have used the micrOmegas v.2.4.5 [19] to calculate thermal relic density and direct detection cross section of the VDM in our model.

In Fig. 1 we show the thermal relic density as a function of the dark matter mass, M_X . For this plot we fixed $m_1 = 125$ GeV, $m_2 = 150$ GeV, $\alpha = \pi/4$ and the purple (blue) line corresponds to $g_X = 0.05$ (0.5). We can see two resonance dips at $M_X = m_i/2$ ($i = 1, 2$). The VDMs can annihilate into the SM particles in the S-wave state, which is different from the singlet fermionic dark matter case studied in [6] where the annihilation occurs in the P-wave state. As a result the annihilation cross section for the vector dark matter is generally $\mathcal{O}(10 - 100)$ larger than that of the SFDM. And the current relic density can be explained more easily even at non-resonance region. (See the blue line in Fig. 1.) The difference between the two curves becomes larger for $M_X > 125$ GeV. This is because the channels $XX \rightarrow H_i H_j$ ($i, j = 1, 2$) which begin to open for $M_X > 125$ GeV are sensitive to g_X and they give larger annihilation cross sections as the coupling g_X increases.

One important effect when considering the full theory, which we found in Ref. [6], is that a generic cancellation occurs in the dark matter and nucleon scattering amplitude, which can not be observed in the effective Lagrangian approach.¹ This is because the transformation matrix between the interaction eigenstates and the mass eigenstates in the scalar sector is an orthogonal matrix. The dark matter and nucleon elastic scattering cross

¹In general the cancellation mechanism can also work in the annihilation process for the relic density. However, the different decay widths for the H_1 and H_2 and/or other processes such as annihilations into scalar particle pairs makes it less effective than in the direct detection process. As a result, the annihilation process and the direct detection process are not strictly proportional to each other in our scenario.

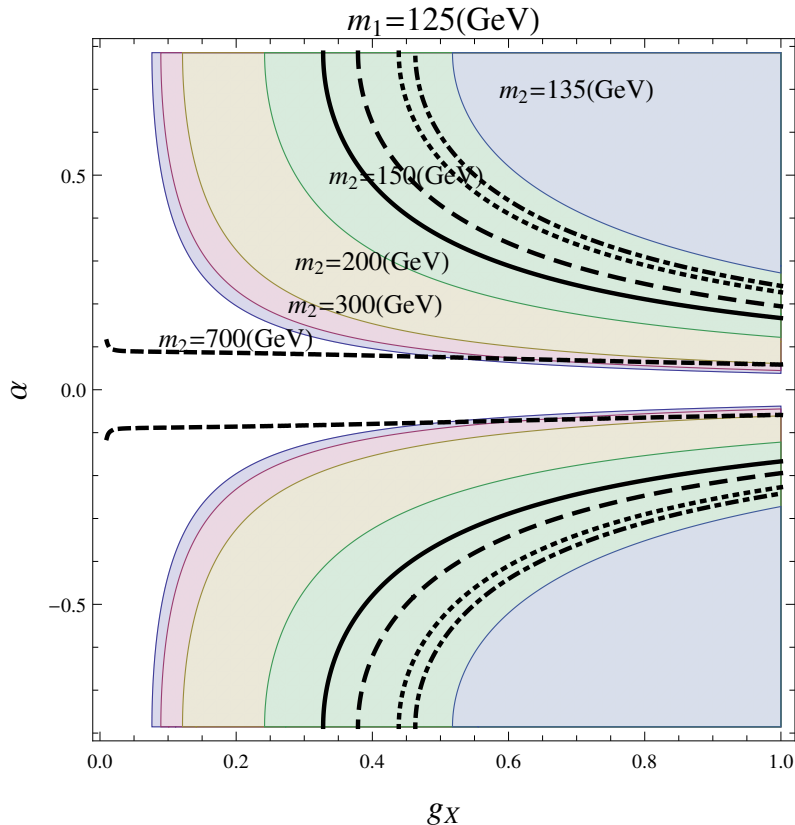


Figure 2. The excluded region in the (g_X, α) -plane. Each colored region is excluded by XENON100 direct detection experiment for the m_2 value given in the plot. We fixed $M_X = 70$ GeV, $m_1 = 125$ GeV. The black solid (dashed, long-dashed, dotted, dot-dashed) curve corresponds to $\Omega_X h^2 = 0.1123$ for $m_2 = 135(150, 200, 300, 700)$ GeV. Therefore, the VDM as light as $M_X = 70$ GeV is allowed by both the relic density and the XENON100 constraints either by the cancellation mechanism for $m_2 = 135$ GeV or by the resonant annihilation for $m_2 = 150$ GeV. The entire region is also allowed by the S, T, U -parameters at 99% confidence level except that only the range $(-0.63, 0.63)$ and $(-0.42, 0.42)$ of α are allowed for $m_2 = 300$ GeV and $m_2 = 700$ GeV, respectively [6].

section is proportional to the following factor:

$$\sigma_p \propto \left| \sum_{i=1,2} \frac{O_{hi} O_{\varphi i}}{q^2 - m_i^2} \right|^2, \quad (3.2)$$

where q is the momentum transfer of the dark matter. When $m_1 \approx m_2$ or $|q^2| \gg m_i^2$, we have $\sigma_p \approx 0$ due to the orthogonality of the mixing matrix O . This cancellation phenomenon is quite similar to the GIM-mechanism [20] in the quark (or lepton) flavor violating neutral current processes. In Fig. 2, we show the excluded region in the (g_X, α) -plane by the non-observation of dark matter by the XENON100 which currently gives the strongest bound on the dark matter direct detection cross section [7]. Each colored region is excluded by XENON100 direct detection experiment for the m_2 value given in the plot. We fixed

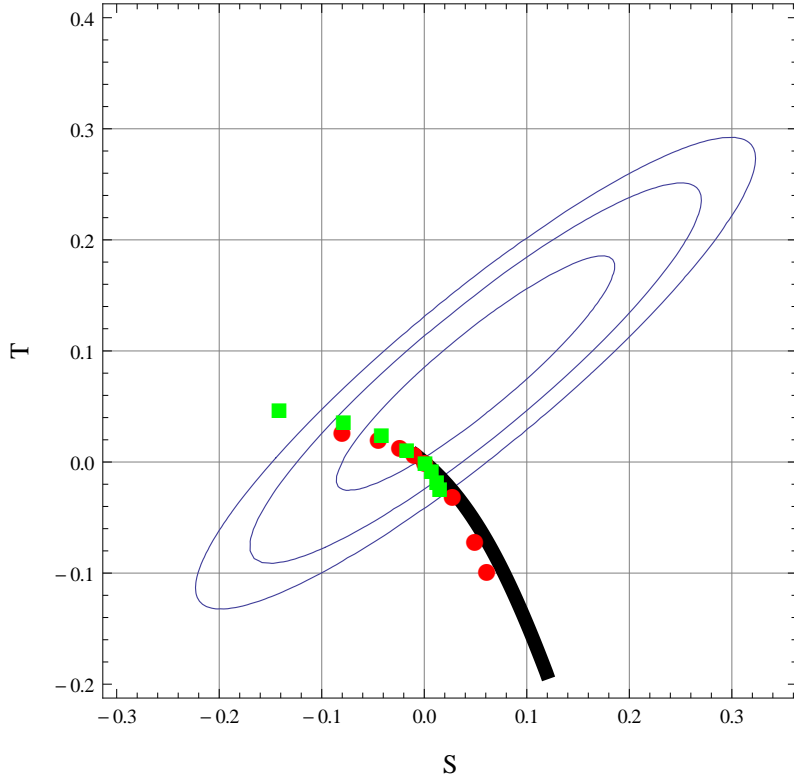


Figure 3. The predictions of (S, T) -parameters in our model for $(m_1, m_2) = (25, 125), (50, 125), (75, 125), (100, 125), (125, 125), (125, 250), (125, 500), (125, 750)$ GeV from above. The green (red) dots are for $\alpha = 45^\circ(20^\circ)$. The thick black line is the prediction of the SM with the m_H in the range $[125, 720]$ GeV. The ellipses represent 68, 95, 99% CL experimental lines from inside out.

$M_X = 70$ GeV, $m_1 = 125$ GeV for the plot. The black solid (dashed, long-dashed, dotted, dot-dashed) curve corresponds to $\Omega_X h^2 = 0.1123$ for $m_2 = 135$ (150, 200, 300, 700) GeV. The case $m_2 = 150$ GeV is close to the resonance ($m_2 = 2M_X$) and shows quite different behavior from the other cases. So the VDM as light as $M_X = 70$ GeV, even if it is off the resonance region, can be consistent with both the relic density and the XENON100 experiment by the cancellation mechanism when H_2 is light. This can be compared with the EFT approach based on the Lagrangian (1.3) where $M_X \lesssim 300$ GeV is already excluded by the direct search limit [2] (See also the blue line in Fig. 6 (a)). The entire region is also allowed by the electroweak precision S, T, U -parameters at 99% confidence level except that only the range $(-0.63, 0.63)$ and $(-0.42, 0.42)$ of α are allowed for $m_2 = 300$ GeV and $m_2 = 700$ GeV, respectively [6].

The predictions of our model on the S, T parameters assuming $U = 0$ are shown in Fig. 3 for the choices $(m_1, m_2) = (25, 125), (50, 125), (75, 125), (100, 125), (125, 125), (125, 250), (125, 500), (125, 750)$ GeV from above. The green (red) dots are for $\alpha = 45^\circ(20^\circ)$. The thick black line is the prediction of the SM with the m_H in the range $[125, 720]$ GeV. The ellipses represent 68, 95, 99% CL experimental lines from inside out.

3.2 Collider phenomenology

Since the scalar sector is extended, the Higgs phenomenology is different from that of the SM. In this subsection we study the possibility that the second Higgs which our model predicts could be discovered at the LHC. We will also see that the combination of the collider signatures and the DM direct searches is robust enough to exclude or confirm our model in the on-going LHC and the next generation DM direct detection experiments.

The signal strength of a scalar boson $H_{i=1,2}$ defined as

$$r_i \equiv \frac{\sigma(pp \rightarrow H_i)B(H_i \rightarrow f_{\text{SM}})}{[\sigma(pp \rightarrow H_i)B(H_i \rightarrow f_{\text{SM}})]^{\text{SM}}} \quad (3.3)$$

can be measured at the LHC. Here $i = 1, 2$ and f_{SM} is a specific SM final state which the scalar boson H_i can decay into. In our model it can be written in terms of $\Gamma_i^{\text{tot,SM}}$ ($i = 1, 2$) which is the total decay width of H_i in the SM assuming H_i is a pure SM Higgs and Γ_i^{tot} which is the total decay width of H_i in our model [6, 11]:

$$r_i = O_{hi}^4 \frac{\Gamma_i^{\text{tot,SM}}}{\Gamma_i^{\text{tot}}}, \quad (3.4)$$

where $O_{h1} = c_\alpha, O_{h2} = s_\alpha$. The total decay widths can be decomposed as

$$\begin{aligned} \Gamma_1^{\text{tot}} &= c_\alpha^2 \Gamma_1^{\text{tot,SM}} + s_\alpha^2 \Gamma_1^{\text{tot,hid}}, \\ \Gamma_2^{\text{tot}} &= s_\alpha^2 \Gamma_2^{\text{tot,SM}} + c_\alpha^2 \Gamma_2^{\text{tot,hid}} + \Gamma(H_2 \rightarrow H_1 H_1), \end{aligned} \quad (3.5)$$

where $\Gamma_i^{\text{tot,hid}}$ is the total decay width of H_i into the hidden sector assuming H_i is a pure SM-singlet scalar. The channel $H_2 \rightarrow H_1 H_1$ opens when $m_2 > 2m_1$. From the eqs. (3.4) and (3.5) it is obvious that $r_i < 1$ in our model. Therefore if the excess of the signal strength in some channels like $H \rightarrow \gamma\gamma$ above the SM prediction at the LHC remains in the future data, our model will either be excluded or need to be extended (two Higgs doublet portal to a hidden sector dark matter, for example). From $r_1 + r_2 < 1$ [6, 11] we obtain $r_2 < 0.3$ for the second Higgs boson, when we identify the observed new boson at 125 GeV (whose signal strength is greater than 0.7 at 2σ level [21]²) as one of the two Higgs-like scalar bosons in our model.

The correlation between r_1 and r_2 can be seen in Fig. 4 where we show only the region $r_1 > 0.7$. For this plot we scanned the parameters g_X, M_X, α, m_2 in the range, $0 < g_X < 1$, $10 \text{ GeV} < M_X < 1000 \text{ GeV}$, $-\pi/2 < \alpha < \pi/2$, $m_1 (= 125 \text{ GeV}) < m_2 < 2000 \text{ GeV}$ for the panel (a), and $10 \text{ GeV} < m_1 < m_2 (= 125 \text{ GeV})$ for the panel (b). All the points pass the constraints: $\Omega_X h^2 < 0.1228$ (the 3σ upper bound of the relic density), the upper bound on the XENON100 direct detection cross section, and the bound on the S, T -parameters at 99% CL. The big (small) points (do not) satisfy the WMAP relic density constraint within 3σ , while the red-(blue-)colored points can (cannot) be probed at the planned XENON1T direct detection experiment [23]. In both plots, the big red points on the straight line, $r_1 + r_2 = 1$, are those with $H_i \rightarrow XX$ and $H_2 \rightarrow H_1 H_1$ suppressed. In the panel (a),

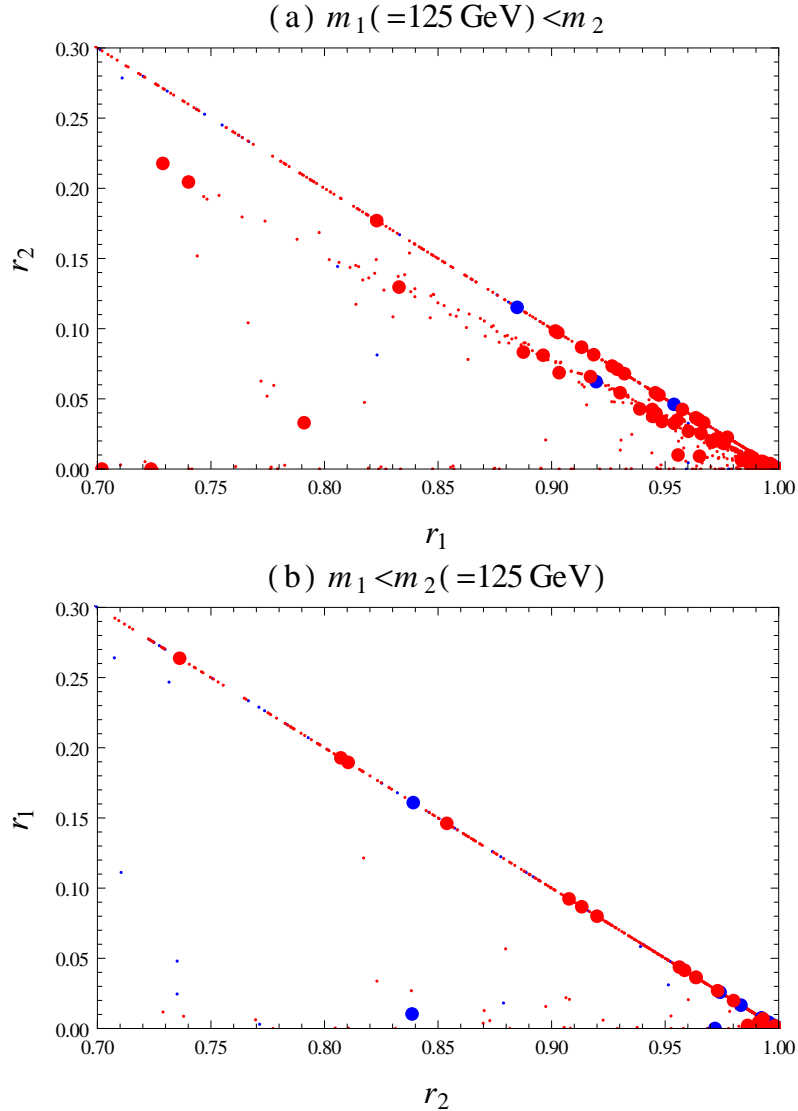


Figure 4. The scatter plot in (a) (r_1, r_2) for $m_1(= 125 \text{ GeV}) < m_2$ and (b) (r_2, r_1) for $m_1 < m_2(= 125 \text{ GeV})$. The big (small) points (do not) satisfy the WMAP relic density constraint within 3σ , while the red-(blue-)colored points can (cannot) be probed at the planned XENON1T direct detection experiment.

the sizable contribution from the $H_2 \rightarrow H_1 H_1$ channel allows the big red points below the $r_1 + r_2 = 1$ line.

In Fig. 5, we show the allowed mixing angle α as a function of the second Higgs mass. We fixed the SM-like Higgs mass to be 125 GeV. Color scheme is the same as Fig. 4 except that black points are excluded by the LHC Higgs search, *i.e.* $r < 0.7$. We can see the maximal mixing angle $\alpha = \pi/4$ (black points near $m_2 \approx 125 \text{ GeV}$) is excluded by the LHC Higgs search. Also the light scalar with mass less than 125 GeV, if exists, should be

²We used only the ATLAS value since there is no combined result. The corresponding value for the CMS can be found in [22]

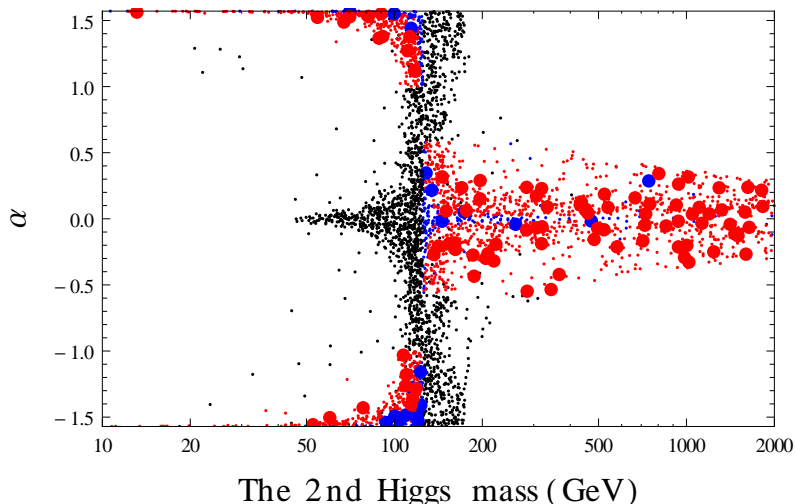


Figure 5. The allowed mixing angle α as a function of the second Higgs mass. We fixed the SM-like Higgs mass to be 125 GeV. The big (small) points (do not) satisfy the WMAP relic density constraint within 3σ , while the red-(blue-)colored points can (cannot) be probed at the planned XENON1T experiment. The black points are excluded by the LHC Higgs search, *i.e.* $r < 0.7$.

singlet-like.

In Fig. 6, we show a scatter plot of σ_p as a function of M_X . The big (small) points (do not) satisfy the WMAP relic density constraint within 3σ , while the red-(black-)colored points gives $r_1 > 0.7$ ($r_1 < 0.7$). The Gray region is excluded by the XENON100 experiment. The dashed line denotes the sensitivity of the next XENON experiment, XENON1T. We note that many points are still allowed by the WMAP relic density constraint, the XENON100 direct detection experiment, and also by the constraint $r_1 > 0.7$ which is in the ball park of the LHC Higgs search bound. On the other hand, the effective field theory approach considered in Ref.s [1] strongly constrains the vector dark matter scenario. We can also see that there is no point below about $M_X \approx 50$ GeV in Fig. 6 (a). It is because the Higgs exchanged dark matter annihilation channel does not allow the resonance and the relic density is larger than the WMAP measurement. Most of the big red points are within the reach of the XENON1T sensitivity, and our model can be tested in the next generation dark matter detection experiment.

3.3 The EFT as a limit of the full theory for $m_2 \rightarrow \infty$

In this subsection we consider the EFT in (1.3) as a limit of the full theory in (2.1) when $m_2 \rightarrow \infty$. We keep finite the full theory parameters: λ_H , λ_Φ , $\lambda_{H\Phi}$ and $M_X (= g_X v_\Phi)$, while taking $v_\Phi \rightarrow \infty$. We trade λ_H for the experimentally measured m_1 using the relation

$$2\lambda_H v_H^2 = m_1^2 + \frac{(\lambda_{H\Phi} v_H v_\Phi)^2}{2\lambda_\Phi v_\Phi^2 - m_1^2}. \quad (3.6)$$

For large v_Φ , m_2 (α) is proportional to v_Φ ($1/v_\Phi$). The light dark matter ($M_X \ll m_2$) is possible when $g_X^2 \ll \lambda_\Phi$. In other words, we should note that the EFT is valid only when

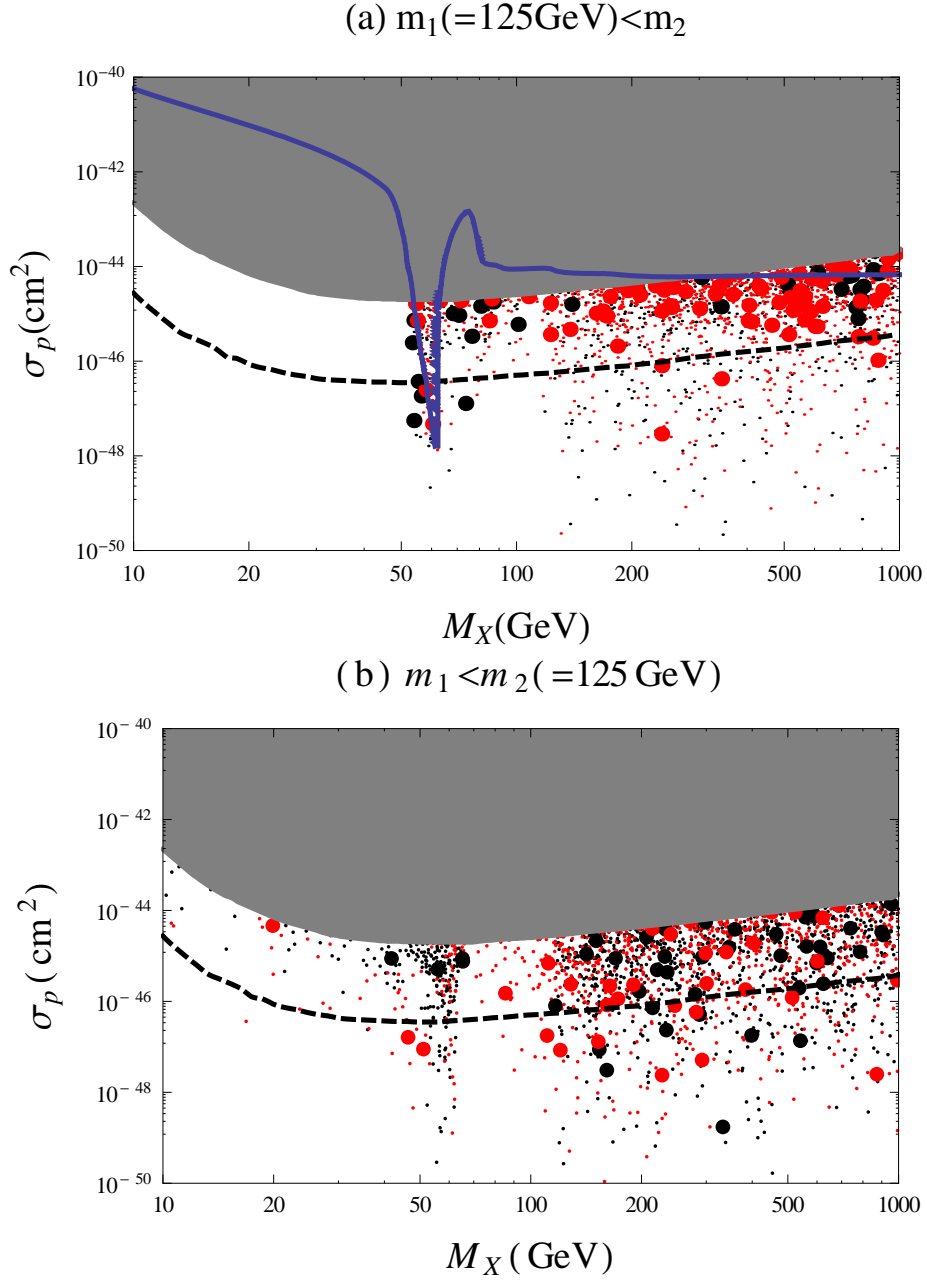


Figure 6. The scatter plot of σ_p as a function of M_X . The big (small) points (do not) satisfy the WMAP relic density constraint within 3σ , while the red-(black-)colored points gives $r_1 > 0.7$ ($r_1 < 0.7$). The gray region is excluded by the XENON100 experiment. The dashed line denotes the sensitivity of the next XENON experiment, XENON1T. The solid blue line in panel (a) represents the prediction of the EFT approach in (1.3).

$m_2 \rightarrow \infty$, $\alpha \rightarrow 0$, $g_X^2 \ll \lambda_\Phi$ and it is a very restricted region. The term $H^\dagger H X_\mu X^\mu$ can be

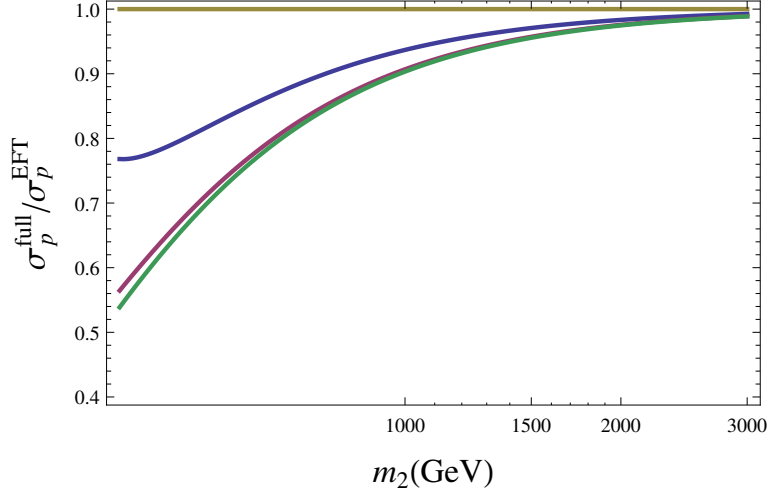


Figure 7. The ratio $\sigma_p^{\text{full}}/\sigma_p^{\text{EFT}}$ as a function of m_2 for several values of $\lambda_{H\Phi}$: $\lambda_{H\Phi} = 0.5, 0.3, 0.1$ (blue, purple, green). We fix $M_X = 300$ GeV, $m_1 = 125$ GeV $\lambda_\Phi = 0.175$.

generated both at tree- and loop-level [2]. Considering the tree-level diagram only, we get

$$\lambda_{HX} = -\frac{2M_X^2 \tilde{\lambda}_{112}}{m_2^2}, \quad (3.7)$$

where $\tilde{\lambda}_{112} \equiv \lambda_{112} c_\alpha / v_\Phi$ and λ_{112} is the $H_1 - H_1 - H_2$ coupling constant given by

$$\lambda_{112} = \lambda_{H\Phi} \left[(c_\alpha^3 - 2c_\alpha s_\alpha^2) v_\Phi + (s_\alpha^3 - 2s_\alpha c_\alpha^2) v_H \right] + 6\lambda_H s_\alpha c_\alpha^2 v_H + 6\lambda_\Phi c_\alpha s_\alpha^2 v_\Phi. \quad (3.8)$$

The elastic cross section σ_p of the VDM X scattering off the proton in the full theory is obtained as

$$\sigma_p^{\text{full}} = \frac{4\mu_X^2}{\pi} \left(\frac{g_X s_\alpha c_\alpha m_p}{2v_H} \right)^2 \left(\frac{1}{m_1^2} - \frac{1}{m_2^2} \right)^2 f_p^2, \quad (3.9)$$

where $\mu_X = M_X m_p / (M_X + m_p)$ and $f_p = \sum_{q=u,d,s} f_q^p + 2/9(1 - \sum_{q=u,d,s} f_q^p) \approx 0.468$ [17]. The EFT predicts the corresponding cross section to be

$$\sigma_p^{\text{EFT}} = \frac{4\mu_X^2}{\pi} \left(\frac{\lambda_{HX} m_p}{4M_X} \right)^2 \frac{1}{m_h^4} f_p^2. \quad (3.10)$$

Using the relations (2.4), (3.7), (3.8) and identifying m_1 and m_h with the observed Higgs mass (~ 125 GeV) in their respective theories, we obtain

$$\frac{\sigma_p^{\text{full}}}{\sigma_p^{\text{EFT}}} = \left(\frac{\lambda_{H\Phi}}{\tilde{\lambda}_{112}} \right)^2. \quad (3.11)$$

This ratio approaches to one as $v_\Phi \rightarrow \infty$. In Fig. 7, we show the ratio $\sigma_p^{\text{full}}/\sigma_p^{\text{EFT}}$ as a function of m_2 to see how quickly the full theory prediction approaches that of the EFT. We choose three different values for $\lambda_{H\Phi}$, $\lambda_{H\Phi} = 0.5, 0.3, 0.1$ (blue, purple, green), and fix

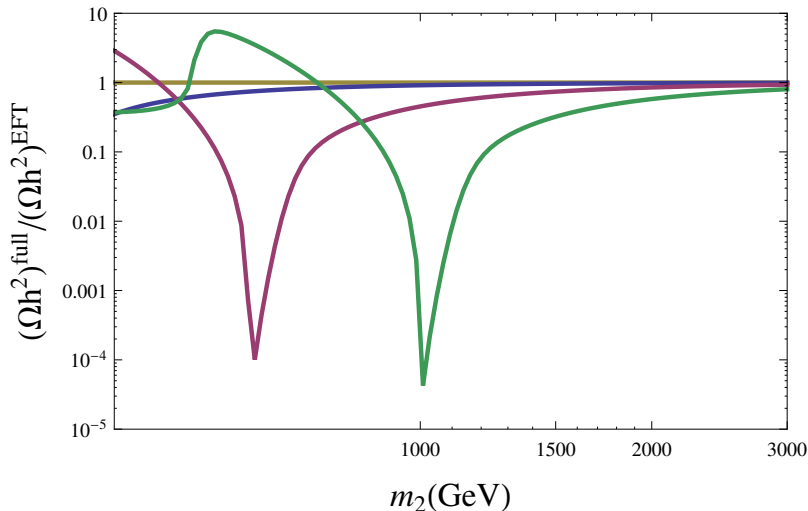


Figure 8. The ratio $(\Omega h^2)^{\text{full}}/(\Omega h^2)^{\text{EFT}}$ as a function of m_2 for several values of M_X : $M_X = 150, 300, 500$ GeV (blue, purple, green). We fix $m_1 = 125$ GeV, $\lambda_\Phi = 0.175$ and $\lambda_{H\Phi} = 0.1$.

other parameters: $M_X = 300$ GeV, $m_1 = 125$ GeV, $\lambda_\Phi = 0.175$. We can see that the EFT predictions agree well with those of the full theory within a few percent when $m_2 \gtrsim 2000$ GeV.

Fig. 8 shows the ratio of relic density predictions in the full theory and the EFT, $(\Omega h^2)^{\text{full}}/(\Omega h^2)^{\text{EFT}}$, as a function of m_2 . Since the dependence on the coupling $\lambda_{H\Phi}$ is not appreciable³, we take several values of M_X instead: $M_X = 150, 300, 500$ GeV (blue, purple, green), although $M_X = 150$ GeV is already excluded by the direct search limit as can be seen in Fig. 6 (a). We fix $m_1 = 125$ GeV, $\lambda_\Phi = 0.175$ and $\lambda_{H\Phi} = 0.1$. There is a sharp increase in the green line at $m_2 \simeq M_X$. This is because the dominant process $XX \rightarrow H_2 H_2$ is kinematically closed at the point and the annihilation cross section decreases abruptly in the full theory. We can also see the resonance effects of the full theory. Both effects are absent in the EFT. We can see that the lighter the DM is, the faster the full theory approaches the EFT.

4 Vacuum stability and perturbativity of Higgs quartic couplings

In this section, we analyze vacuum stability and perturbativity of Higgs quartic couplings. To make the Higgs potential be bounded-from-below, we require

$$\lambda_H > 0, \quad \lambda_\Phi > 0, \quad -2\sqrt{\lambda_H \lambda_\Phi} < \lambda_{H\Phi}, \quad (4.1)$$

where the last condition applies for $\lambda_{H\Phi} < 0$. We also require

$$\det M_{\text{Higgs}}^2 = \det \begin{pmatrix} 2\lambda_H v_H^2 & \lambda_{H\Phi} v_H v_\Phi \\ \lambda_{H\Phi} v_H v_\Phi & 2\lambda_\Phi v_\Phi^2 \end{pmatrix} = (4\lambda_H \lambda_\Phi - \lambda_{H\Phi}^2) v_H^2 v_\Phi^2 > 0. \quad (4.2)$$

³This is partly because the $XX \rightarrow H_2 \rightarrow H_1 H_1$ process is important and the amplitudes of which are exactly the same in both the full theory and the EFT.

Since there is additional direction of Φ , the Higgs potential can have minima other than our EW vacuum. In the following, we investigate whether the EW vacuum is global or not. We closely follow the analysis done in Ref. [11].

The tree-level effective potential takes the $U(1)_X$ symmetric form

$$V_0(\varphi_H, \varphi_\Phi) = \frac{\lambda_H}{4}(\varphi_H^4 - 2v_H^2\varphi_H^2) + \frac{\lambda_\Phi}{4}(\varphi_\Phi^4 - 2v_\Phi^2\varphi_\Phi^2) + \frac{\lambda_{H\Phi}}{4}(\varphi_H^2\varphi_\Phi^2 - \varphi_H^2v_\Phi^2 - v_H^2\varphi_\Phi^2), \quad (4.3)$$

where φ_H and φ_Φ are spacetime-independent classical fields. Following the Refs. [24, 25], we define the various vacua as follows:

$$\text{EW} : v_H = 246 \text{ GeV}, \quad v_\Phi \neq 0, \quad (4.4)$$

$$\text{SYM} : v_H = v_\Phi = 0, \quad (4.5)$$

$$\text{I} : v_H = 0, \quad v_\Phi \neq 0, \quad (4.6)$$

$$\text{II} : v_H \neq 0, \quad v_\Phi = 0. \quad (4.7)$$

Unlike the general Higgs potential, only nontrivial phase may be the I-phase. Such a minimum is given by

$$\bar{v}_\Phi = \pm \sqrt{v_\Phi^2 + \frac{\lambda_{H\Phi}}{2\lambda_\Phi} v_H^2}. \quad (4.8)$$

The differences of vacuum energies of the I- and the EW phases is

$$\begin{aligned} V_0^{(\text{I})}(0, \bar{v}_\Phi) - V_0^{(\text{EW})}(v_H, v_\Phi) &= \frac{\lambda_H}{4} v_H^4 + \frac{\lambda_{H\Phi}}{4} v_H^2 v_\Phi^2 - \frac{\lambda_\Phi}{4} (\bar{v}_\Phi^4 - v_\Phi^4) \\ &= \frac{1}{16\lambda_\Phi} (4\lambda_H\lambda_\Phi - \lambda_{H\Phi}^2) v_H^4, \end{aligned} \quad (4.9)$$

where we have used Eq. (4.8) in the second line. Therefore, as long as Eqs. (4.1) and (4.2) are satisfied, the EW vacuum is always the global minimum. Note that this is not the case for the generic Higgs potential [11].

Although the EW vacuum is stable at the EW scale, its stability up to Planck scale ($M_{\text{Pl}} \simeq 1.22 \times 10^{19}$ GeV) is nontrivial question since a renormalization group (RG) effect of the top quark can drive λ_H negative at certain high-energy scale, leading to an unbounded-from-below Higgs potential or a minimum that may be deeper than the EW vacuum. We will work out this question by solving RG equations with respect to the Higgs quartic couplings and the $U(1)_X$ gauge coupling. The one-loop β functions of those couplings are listed in Appendix A. In addition to the vacuum stability, we also take account of the perturbativity of the couplings. To be specific, we impose $\lambda_i(Q) < 4\pi$ ($i = H, H\Phi, \Phi$) and $g_X^2(Q) < 4\pi$ up to $Q = M_{\text{Pl}}$.

Fig. 9 shows the vacuum stability and the perturbativity constraints in the α - m_2 plane. We take $m_1 = 125$ GeV, $g_X = 0.05$, $M_X = m_2/2$ and $v_\Phi = M_X/(g_X Q_\Phi)$. The vacuum stability constraint is denoted by red line; i.e., the region above the red line is allowed for $\alpha > 0$, and it is the other way around for $\alpha < 0$. The perturbativity requirement is represented by blue line; i.e., the region below the blue line is allowed for $\alpha > 0$, and it is the

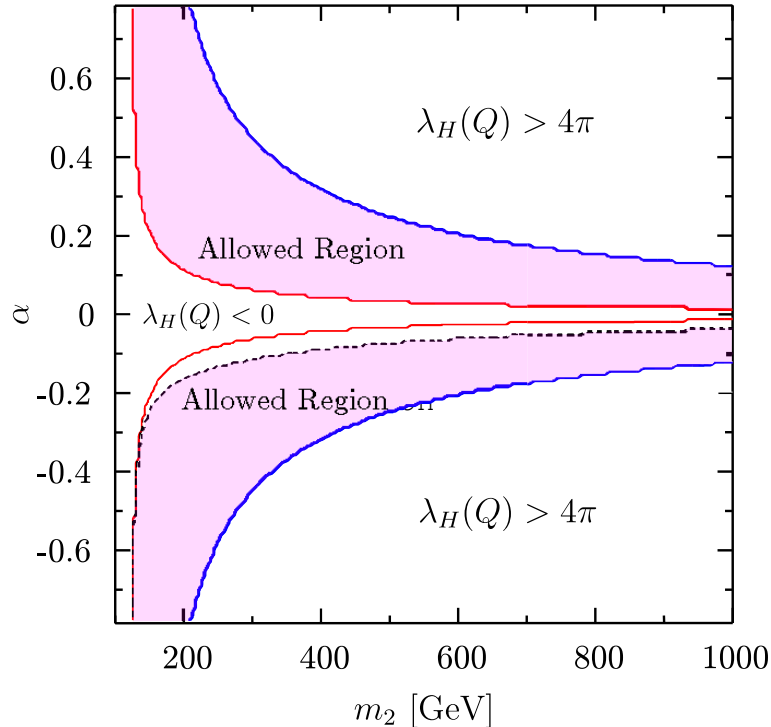


Figure 9. The vacuum stability and perturbativity constraints in the α - m_2 plane. We take $m_1 = 125$ GeV, $g_X = 0.05$, $M_X = m_2/2$ and $v_\Phi = M_X/(g_X Q_\Phi)$.

other way around for $\alpha < 0$. For $\alpha < 0$, the region above the dotted black line is excluded by Eq. (4.1). Putting all together, for $\alpha > 0$ the region between the red and blue lines is allowed while for $\alpha < 0$ the region between the dotted black and blue lines is allowed. It should be noted that since the coefficient of $\lambda_{H\Phi}$ in β_{λ_H} is doubled in comparison with the real singlet case, the improvement of the vacuum stability by the increase of $\lambda_{H\Phi}$ or, equivalently α , is more effective. However, unlike the general Higgs potential involving explicit $U(1)_X$ breaking terms, the EW vacuum cannot be stable up to Planck scale if α is exactly zero.

In Fig. 10, we show the vacuum stability and perturbativity constraints in the M_X - m_2 plane. We fix $\alpha = 0.1$ varying g_X , i.e., $g_X = 0.1$ (Left Panel) and 0.5 (Right Panel). Once g_X is fixed, the small M_X is realized by a small v_Φ . In such a case, the large m_2 is possible only by a large λ_Φ since $m_2 \simeq \sqrt{2\lambda_\Phi}v_\Phi$ for a small α . This explains the regions excluded by $\lambda_\Phi(Q) > 4\pi$ in both plots. Indeed, the $g_X = 0.5$ case yields the severer constraints. As for the vacuum stability constraint, the change of g_X has little effect on it, which can be understood from the expression of β_{λ_H} , Eq. (A.2).

5 Conclusions

In this paper, we revisited the Higgs portal vector dark matter including the hidden sector Higgs field Φ that provides the vector dark matter mass. Including the hidden sector Higgs field makes the model renormalizable and unitary. The constraint from direct detection

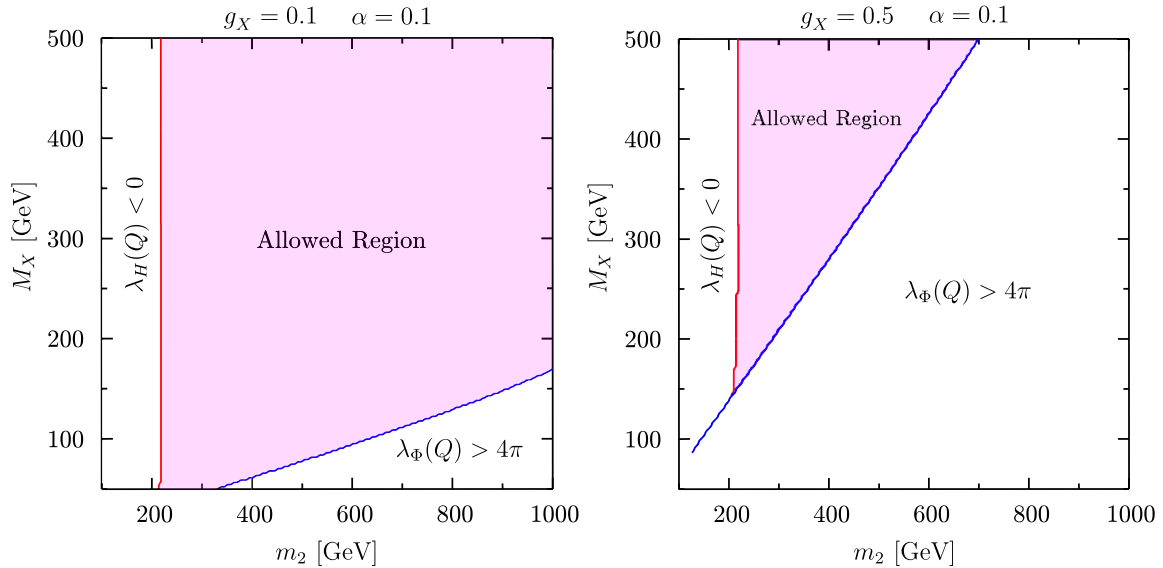


Figure 10. The vacuum stability and perturbativity constraints in the M_X - m_2 plane. We set $g_X = 0.1$ (Left Panel) and 0.5 (Right Panel) with being $\alpha = 0.1$.

cross section (XENON100) still allows a large parameter space in this model. On the contrary to some claims that the Higgs portal dark matter model is strongly constrained by XENON100 data, we showed that the model is still viable. It is crucial to work with a model that is renormalizable, and not with effective lagrangian, as in the Higgs portal fermion DM model in Ref. [6, 11] Including the hidden sector Higgs field also improves the vacuum stability of the model for $m_H = 125$ GeV upto the Planck scale as in Ref. [11]. Our model can be tested at colliders by searching for the 2nd Higgs boson and/or the signal strength of the 125 GeV Higgs boson. It would take long in order to observe the 2nd Higgs boson since its signal strength is smaller than 0.3. In our model, r_i is universally suppressed relative to the SM case for all channels. This could be a useful criterion when the signal strengths of 125 GeV Higgs boson are measured with smaller uncertainties. If r_i is not universally suppressed or larger than one, then our model shall be excluded.

Acknowledgments

We are grateful to Yasaman Farzan for bringing Ref. [15] to our attention. This work is supported in part by NRF Research Grant 2012R1A2A1A01006053 (PK and SB), and by SRC program of NRF Grant No. 20120001176 funded by MEST through Korea Neutrino Research Center at Seoul National University (PK). WIP is supported in part by Basic Science Research Program through the National Research Foundation of Korea(NRF) funded by the Ministry of Education, Science and Technology(2012-0003102).

A One-loop β functions of Higgs quartic couplings

The renormalization group equation and the β functions are given by

$$\frac{d\lambda(t)}{d\log(Q)} = \beta_\lambda, \quad (\text{A.1})$$

where

$$\beta_{\lambda_H} = \frac{1}{16\pi^2} \left[24\lambda_H^2 + \lambda_{H\Phi}^2 - 6y_t^4 + \frac{3}{8} \left\{ 2g_2^4 + (g_2^2 + g_1^2)^2 \right\} - \lambda_H \left\{ 3(3g_2^2 + g_1^2) - 12y_t^2 \right\} \right], \quad (\text{A.2})$$

$$\beta_{\lambda_{H\Phi}} = \frac{1}{16\pi^2} \left[2\lambda_{H\Phi}(6\lambda_H + 4\lambda_\Phi + 2\lambda_{H\Phi}) - \lambda_{H\Phi} \left\{ \frac{3}{2}(3g_2^2 + g_1^2) - 6y_t^2 + 6g_X^2 Q_\Phi^2 \right\} \right], \quad (\text{A.3})$$

$$\beta_{\lambda_\Phi} = \frac{1}{16\pi^2} \left[2(\lambda_{H\Phi}^2 + 10\lambda_\Phi^2 + 3g_X^4 Q_\Phi^4) - 12\lambda_\Phi g_X^2 Q_\Phi^2 \right], \quad (\text{A.4})$$

$$\beta_{g_X} = \frac{1}{16\pi^2} \frac{1}{3} g_X^3 Q_\Phi^2. \quad (\text{A.5})$$

References

- [1] S. Kanemura, S. Matsumoto, T. Nabeshima and N. Okada, Phys. Rev. D **82** (2010) 055026 [arXiv:1005.5651 [hep-ph]];
- [2] O. Lebedev, H. M. Lee and Y. Mambrini, Phys. Lett. B **707** (2012) 570 [arXiv:1111.4482 [hep-ph]];
- [3] A. Djouadi, O. Lebedev, Y. Mambrini and J. Quevillon, Phys. Lett. B **709** (2012) 65 [arXiv:1112.3299 [hep-ph]].
- [4] L. Lopez-Honorez, T. Schwetz and J. Zupan, Phys. Lett. B **716** (2012) 179 [arXiv:1203.2064 [hep-ph]].
- [5] Y. G. Kim, K. Y. Lee and S. Shin, JHEP **0805**, 100 (2008) [arXiv:0803.2932 [hep-ph]].
- [6] S. Baek, P. Ko and W. -I. Park, JHEP **1202** (2012) 047 [arXiv:1112.1847 [hep-ph]].
- [7] E. Aprile *et al.* [XENON100 Collaboration], Phys. Rev. Lett. **109** (2012) 181301 [arXiv:1207.5988 [astro-ph.CO]].
- [8] Z. Ahmed *et al.* [CDMS and EDELWEISS Collaborations], Phys. Rev. D **84**, 011102 (2011) [arXiv:1105.3377 [astro-ph.CO]].
- [9] G. Aad *et al.* [ATLAS Collaboration], Phys. Lett. B **716**, 1 (2012) [arXiv:1207.7214 [hep-ex]].
- [10] S. Chatrchyan *et al.* [CMS Collaboration], Phys. Lett. B **716**, 30 (2012) [arXiv:1207.7235 [hep-ex]].
- [11] S. Baek, P. Ko, W. -I. Park and E. Senaha, JHEP **1211**, 116 (2012) [arXiv:1209.4163 [hep-ph]].
- [12] O. Lebedev, Eur. Phys. J. C **72**, 2058 (2012) [arXiv:1203.0156 [hep-ph]].
- [13] J. Elias-Miro, J. R. Espinosa, G. F. Giudice, H. M. Lee and A. Strumia, JHEP **1206**, 031 (2012) [arXiv:1203.0237 [hep-ph]].

- [14] Work in preparation.
- [15] Y. Farzan and A. R. Akbarieh, JCAP **1210** (2012) 026 [arXiv:1207.4272 [hep-ph]].
- [16] T. Hambye, JHEP **0901** (2009) 028 [arXiv:0811.0172 [hep-ph]]; T. Hambye and M. H. G. Tytgat, Phys. Lett. B **683** (2010) 39 [arXiv:0907.1007 [hep-ph]]. H. Zhang, C. S. Li, Q. -H. Cao and Z. Li, Phys. Rev. D **82** (2010) 075003 [arXiv:0910.2831 [hep-ph]]; C. Arina, T. Hambye, A. Ibarra and C. Weniger, JCAP **1003** (2010) 024 [arXiv:0912.4496 [hep-ph]]. J. L. Diaz-Cruz and E. Ma, Phys. Lett. B **695** (2011) 264 [arXiv:1007.2631 [hep-ph]]; S. Bhattacharya, J. L. Diaz-Cruz, E. Ma and D. Wegman, Phys. Rev. D **85** (2012) 055008 [arXiv:1107.2093 [hep-ph]]. T. Abe, M. Kakizaki, S. Matsumoto and O. Seto, Phys. Lett. B **713** (2012) 211 [arXiv:1202.5902 [hep-ph]].
- [17] G. Belanger, F. Boudjema, A. Pukhov and A. Semenov, Comput. Phys. Commun. **180**, 747 (2009) [arXiv:0803.2360 [hep-ph]].
- [18] E. Komatsu *et al.* [WMAP Collaboration], Astrophys. J. Suppl. **192**, 18 (2011) [arXiv:1001.4538 [astro-ph.CO]].
- [19] G. Belanger, F. Boudjema, P. Brun, A. Pukhov, S. Rosier-Lees, P. Salati and A. Semenov, Comput. Phys. Commun. **182** (2011) 842 [arXiv:1004.1092 [hep-ph]].
- [20] S. L. Glashow, J. Iliopoulos and L. Maiani, Phys. Rev. D **2**, 1285 (1970).
- [21] [ATLAS Collaboration], ATLAS-CONF-2012-162.
- [22] [CMS Collaboration], CMS-HIG-12-045.
- [23] E. Aprile [XENON1T Collaboration], arXiv:1206.6288 [astro-ph.IM].
- [24] K. Funakubo, S. Tao and F. Toyoda, Prog. Theor. Phys. **114** (2005) 369 [hep-ph/0501052].
- [25] K. Cheung, T. -J. Hou, J. S. Lee and E. Senaha, Phys. Rev. D **82** (2010) 075007 [arXiv:1006.1458 [hep-ph]].